



HAL
open science

Mapping 2-D Bedload Rates Throughout a Sand-Bed River Reach From High-Resolution Acoustical Surveys of Migrating Bedforms

Jérôme Le Coz, Emeline Perret, Benoît Camenen, David J Topping, Daniel D Buscombe, Kate C P Leary, Guillaume Dramais, Paul E Grams

► **To cite this version:**

Jérôme Le Coz, Emeline Perret, Benoît Camenen, David J Topping, Daniel D Buscombe, et al.. Mapping 2-D Bedload Rates Throughout a Sand-Bed River Reach From High-Resolution Acoustical Surveys of Migrating Bedforms. *Water Resources Research*, 2023, 58 (11), pp.e2022WR032434. 10.1029/2022WR032434 . hal-03909901

HAL Id: hal-03909901

<https://hal.science/hal-03909901>

Submitted on 6 Feb 2023

HAL is a multi-disciplinary open access archive for the deposit and dissemination of scientific research documents, whether they are published or not. The documents may come from teaching and research institutions in France or abroad, or from public or private research centers.

L'archive ouverte pluridisciplinaire **HAL**, est destinée au dépôt et à la diffusion de documents scientifiques de niveau recherche, publiés ou non, émanant des établissements d'enseignement et de recherche français ou étrangers, des laboratoires publics ou privés.

Water Resources Research

RESEARCH ARTICLE

10.1029/2022WR032434

Key Points:

- We introduce a method for mapping bedload fluxes using repeat, high-resolution acoustical bathymetric surveys of a river reach
- The method combines cross-correlation velocimetry and local analysis of individual bedforms along their direction of travel
- Application to the Colorado River in Grand Canyon provides a proof-of-concept and shows the spatio-temporal variability of local bedload

Supporting Information:

Supporting Information may be found in the online version of this article.

Correspondence to:

J. Le Coz,
jerome.lecoz@inrae.fr

Citation:

Le Coz, J., Perret, E., Camenen, B., Topping, D. J., Buscombe, D. D., Leary, K. C. P., et al. (2022). Mapping 2-D bedload rates throughout a sand-bed river reach from high-resolution acoustical surveys of migrating bedforms. *Water Resources Research*, 58, e2022WR032434. <https://doi.org/10.1029/2022WR032434>

Received 28 MAR 2022

Accepted 1 NOV 2022

Mapping 2-D Bedload Rates Throughout a Sand-Bed River Reach From High-Resolution Acoustical Surveys of Migrating Bedforms

Jérôme Le Coz¹ , Emeline Perret^{1,2}, Benoît Camenen¹ , David J. Topping³ , Daniel D. Buscombe⁴ , Kate C. P. Leary⁵, Guillaume Dramais¹, and Paul E. Grams³

¹UR RiverLy, INRAE, Lyon-Villeurbanne, France, ²Compagnie nationale du Rhône, Lyon, France, ³U.S. Geological Survey, Southwest Biological Science Center, Grand Canyon Monitoring and Research Center, Flagstaff, AZ, USA, ⁴Marda Science, Flagstaff, AZ, USA, ⁵Department of Earth and Environmental Sciences, New Mexico Institute of Mining and Technology, Socorro, NM, USA

Abstract This paper introduces a method for determining spatially-distributed, 2-D bedload rates using repeat, high-resolution surveys of the bed topography. As opposed to existing methods, bedform parameters and bedload rates are computed from bed elevation profiles interpolated along the local bedform velocities. The bedform velocity fields are computed applying Large-Scale Particle Image Velocimetry, initially developed for surface velocity measurements, to pairs of successive Digital Elevation Models (DEMs). The bathymetry data are interpolated along the direction of each bedform velocity and the mean height of the closest bedform is computed. The dune shape factor is also evaluated along each bedform direction of travel. The local bedload fluxes can be computed by multiplying the bedform velocity by its mean height averaged over the successive two DEMs, and they can be time-averaged over a series of DEM pairs. This method is applied to a high-resolution acoustical survey of an approximately 300 m long by 40 m wide reach of the Colorado River in Grand Canyon upstream from Diamond Creek, USA. The repeat period was about 6–10 min and bed elevation was interpolated every 0.25 m. The obtained results provide insight to the spatial and temporal variability of bedload rates, bedform parameters and bedload fluxes through cross-sections. The method can be applied to other repeated acoustical surveys of river reaches provided that the space and time resolutions are high enough to capture the local movement of bedforms.

1. Introduction

Measuring bedload in sand-bed channels is important for a number of river and coastal management issues (e.g., sediment budget, channel stability, navigation, ecological habitat, coastal retreat) but it remains a challenging operation. Due to technical difficulties, cost, and field hazards, manual sampling techniques are often replaced by surrogate techniques such as dune-tracking from acoustical sounding of the bed topography. Bedform characteristics such as bedform height, wavelength, and velocity can be determined with reasonable accuracy, then used to determine bedload if two successive surveys of bed elevation are available. Based on the Exner equation for sediment continuity, the mean bedload rate q_b over a bedform wave length can be expressed as (Simons et al., 1965):

$$q_b = (1 - p)V_b H_b + q_{b,0} \quad (1)$$

where p is the bedform porosity, V_b is the bedform velocity, H_b is the mean bedform height (thickness) and $q_{b,0}$ is a constant bedload rate that may be interpreted as the transport rate below the bedform baseline (Simons et al., 1965) or as the fraction of bed material load that moves intermittently in near-bed suspension (McElroy & Mohrig, 2009). Traditionally, the mean bedform height is computed as $H_b = \alpha_b H_{b,\max}$ where $H_{b,\max}$ is the crest-to-trough height of bedforms and α_b is the bedform shape factor. Most often, dunes are assumed to be triangular in shape, hence $\alpha_b = 0.5$.

A number of methods for determining bedform characteristics from a bed-elevation profile (or longitudinal transect) exist (see van der Mark & Blom, 2007 for a review). The detection of bedforms can be based on either manually selected crests and troughs, local extremes, or zero crossings in the detrended bed-elevation profile. These methods come with a variable degree of subjectivity, usually requiring some choices and thresholds to be set to avoid including smaller, superimposed bedforms or minor variations in the bed-elevation profile. Traditionally,

bedform velocities are determined from the evolution of crest lines or other bedform patterns from time to time that are detected either manually or through cross-correlation of bed-elevation profiles (van den Berg, 1987; Hoekstra et al., 2004).

Modern depth sounding technologies like multibeam echosounders, acoustic Doppler current profilers and stereophotogrammetry have been increasingly used to improve the resolution and accuracy of dune-tracking, in both laboratory and field conditions. The principle (cf., Equation 1) introduced by Simons et al. (1965) has been applied to unidirectional bed-elevation profiles (or longitudinal transects) by for example, Dinehart (2002); van der Mark et al. (2008); Claude et al. (2012); Leary and Buscombe (2020); Le Guern et al. (2021). Alternatively, the observed scour (Abraham et al., 2011) or deposition (Nittrouer et al., 2008) volume in a longitudinal panel between successive surveys can be related to bedload transport rate (McAlpin et al., 2022). Abraham et al. (2011) demonstrated that this approach is mathematically equivalent to the approach based on Simons et al. (1965) equation, as soon as scour and deposition volumes are balanced and the distance between successive scour and deposition zones has the same order of magnitude as bedload travel distance. As the applications of both approaches intend to quantify bedload discharge in a river reach, the cross-stream component of bedload is not determined. Along-channel bed-elevation profiles or bathymetric panels are used to establish streamwise bedload transport rates which may be laterally averaged in some cases.

Very few studies have assessed the bedload spatio-temporal variability at the bedform scale (Muste et al., 2016; Strick et al., 2019). Muste et al. (2016) applied Large-Scale Particle Image Velocimetry (LSPIV) to map bedform velocities from repeat bathymetric surveys, a method they called Acoustic Mapping Velocimetry, also introduced by Kim et al. (2016) and by You et al. (2021) who recently proposed general guidelines for its application to field surveys. However, to compute bedload rates, they used the mean bedform heights computed over along-channel profiles and did not determine the cross-stream component of bedload. Crests and troughs of bedforms were selected manually, and the mean dune height was established as the average of the vertical distances from the crest to the upstream and downstream troughs. The dunes were assumed triangular ($\alpha_b = 0.5$). Image cross-correlation techniques have also been applied by Tsubaki et al. (2018) to experimental flume data in order to compute the local velocities of individual bedforms. However, bedload transport was not computed. On the other hand, Strick et al. (2019) computed locally-oriented bedload rates based on aerial imagery of dune migration in the sandy braided South Saskatchewan River, Canada. But the characteristics and the movement of the bedforms were determined manually over an irregular mesh.

We present a method for determining spatially distributed bedload fluxes using repeat, high-resolution surveys of the bed topography. The method can be seen as an extension of the approach of Muste et al. (2016) and Kim et al. (2016) where the characteristics of bedforms are determined locally and automatically so that 2-D bedload components can be computed and mapped. This method consists of evaluating, for each time step and each location, the bedform velocity (using cross-correlation image velocimetry tools) and the bedform mean height along the velocity direction to compute the instantaneous local bedload fluxes. Information such as the bedform shape factors or their lengths are retrieved as well. While any method for determining the bedform characteristics could be used, an objective and semi-automated method is introduced to ensure that the detected bedforms are consistent with the associated bedform-velocity measurements. This method is applied to a high-resolution acoustical survey of a reach of the Colorado River in Grand Canyon upstream from Diamond Creek, where migrating dunes were tracked with high spatio-temporal resolution (Leary & Buscombe, 2020).

2. Site and Data

2.1. The Colorado River Reach

Our study site is located on the Colorado River in Grand Canyon National Park, Arizona (USA), near the U.S. Geological Survey (USGS) Colorado River above Diamond Creek near Peach Springs, Arizona, 09404200 stream-flow gaging station, herein referred to as the Above Diamond Creek gage (Figure 1). This study site is located 388 km downstream from Glen Canyon Dam, which has regulated this segment of the Colorado River since 1963. Based on 31 water years of record (1990–2020), the mean discharge at this stream gage was 422 m³/s. The maximum discharge at this gage since 1963 was roughly 2,750 m³/s. Sand concentration and median grain size have been recorded continuously at 15-min intervals by inverting the acoustic backscatter signal of side-looking acoustic-Doppler profilers, using the method presented by Topping and Wright (2016).

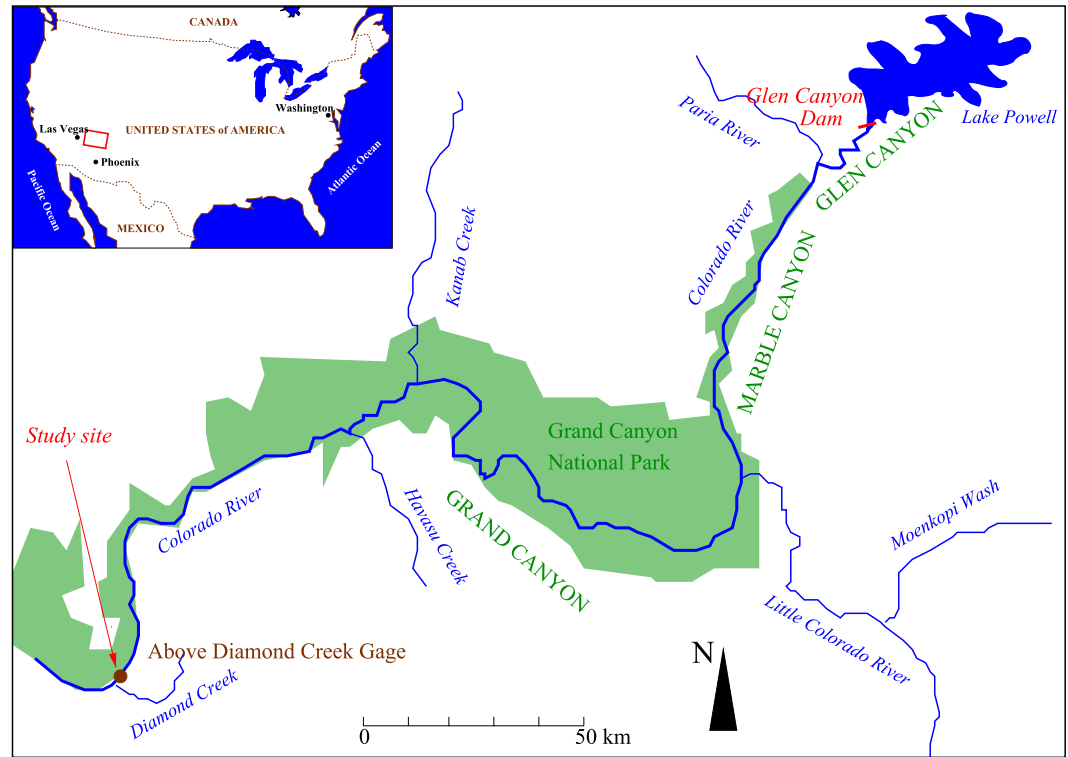


Figure 1. Location map of the Colorado River from Lake Powell to Diamond Creek. The red box on the map of the United States shows the location of the expanded region. The study site is near the U.S. Geological Survey (USGS) Colorado River above Diamond Creek near Peach Springs, Arizona, 09404200 streamflow gaging station.

After the closure of Glen Canyon Dam, sand supply limitation has led to substantial erosion of the bed and depletion of iconic and ecologically valuable sand bars (Rubin et al., 2002). During floods, tributaries like the Paria River still provide limited sand inputs, which travel down the Colorado River as an elongating sediment wave with a finer front (Topping et al., 2000, 2021). Sediment travels in suspension as well as bedload with migrating dunes. Bed material tends to be well-sorted medium sand.

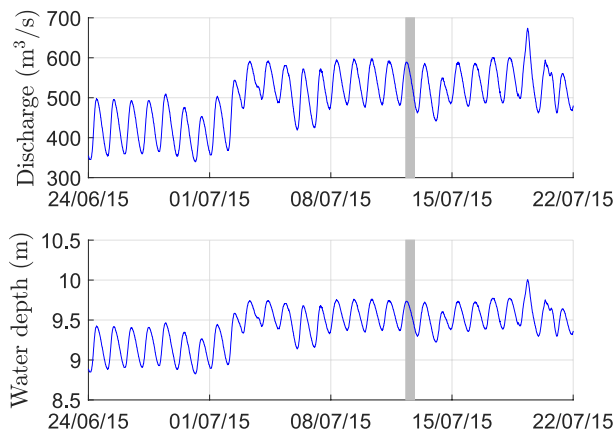


Figure 2. Water discharge and mean water depth time series recorded at the U.S. Geological Survey (USGS) Colorado River Above Diamond Creek near Peach Springs, Arizona, 09404200 streamflow gaging station in June-July 2015 (the gray area corresponds to the 12 July 2015 survey).

2.2. Data Set

We use a high spatio-temporal resolution repeat bed-elevation survey of a 300 m long by 40 m wide reach with migrating dunes upstream from the Above Diamond Creek gage. During two campaigns in March and July 2015, repeated bed-elevation mapping was achieved every 6–10 min for approximately 12 hr using a Teledyne-Reson 7125 multibeam echosounder, and accurately positioned using a vessel-mounted inertial navigation system and a robotic total station. The measurement procedures and the data are described by Kaplinski et al. (2017), Leary and Buscombe (2020), and Ashley et al. (2020). They explain the purpose of their experiment design and the implications of the spatio-temporal scales and resolutions of the survey for the analysis of bedform dynamics. As a typical example of the application, we focus on the data of the 12 July 2015 survey conducted during a decreasing discharge around 566 m³/s on average (Figure 2). The water surface elevation drop was about 9 cm over the 140 m reach upstream from the gage, or a slope of 0.0006.

The mean water depth h was computed from the stage-discharge relation at the station (cf. Camenen et al. (2019)). A power-law representing the channel control (cf. Le Coz et al. (2014)) was calibrated against the stage-discharge measurements:

$$Q = a(z_w - b)^c \quad (2)$$

where Q is the discharge, z_w is the water surface elevation (or stage), a , b , and c are the coefficient, offset and exponent of the control, respectively ($a = 78$, $b = 6.7$, $c = 1.7$). The calibrated value of the offset b corresponds to the cease-to-flow level of the equivalent rectangular channel control. The mean water depth $h = z_w - b + \Delta z$ was computed from the stage records; the correction constant $\Delta z = -0.25$ m was calibrated to fit the values reported by Guala et al. (2020) for the average water depth along the channel centerline. The mean water depth was 9.76 m at the highest flow (09:01 survey, 589 m³/s), 9.20 m at the lowest flow (20:41 survey, 487 m³/s) and 9.50 m on average.

Digital Elevation Models (DEMs) of the riverbed were produced by interpolating bed-elevation measurements over a 0.25 m \times 0.25 m grid. The DEM times are the start times of each survey. Each survey consisted of two passes of the boat, starting and ending at the downstream end of the reach. The two surveys were merged to get full coverage. Longer gaps every hour or so were due to pauses necessary to re-level the robotic total station used to position the boat, and to correct for errors due to large temperature changes inside the canyon. Kaplinski et al. (2017) reported a high precision, with mean cell-elevation standard deviation of 0.012 m computed over immobile rocks. The data were made publicly available by Leary (2018). We assume grain-size percentiles $d_{50} = 0.27$ mm and $d_{84} = 0.41$ mm based on cross-section-averaged bed-sand data from the USGS Grand Canyon Monitoring and Research Center (GCMRC) database collected at the Above Diamond Creek gage on 22 June 2015 (https://www.gcmrc.gov/discharge_qw_sediment/).

3. Method

3.1. Computing Bedform Velocity Using Image Velocimetry

The velocity of bedforms is computed using Large Scale Particle Image Velocimetry (LSPIV, Fujita et al. (1998)), a cross-correlation method usually applied to measure the surface velocities of open-channel flows in-situ or in laboratory experiments. In LSPIV, square gray-scale image patterns are tracked from one image to the next to determine the most probable displacement of surface water over the known time interval. The same velocimetry principle can be applied to other types of moving objects provided that visible and stable tracers are spatially distributed and the movement occurs in a plane. These assumptions are acceptable in the case of the bathymetric survey of bedforms migrating along the bottom of a river channel. The successive DEMs are converted into 256 grayscale levels over the fixed range between the minimum and maximum elevations (Figure 3a). Converting the data from float to integer numbers does not affect correlation results because the elevation resolution is still a small fraction of the dune heights. Indeed, given that the elevation range is approximately 8 m, each of the 256 grayscale levels represents 0.03 m increment.

The DEMs are imported as gray-scale images in the free software Fudaa-LSPIV to perform the next computational steps (see Le Coz et al., 2014; Jodeau et al., 2020, for details about the software). LSPIV is applied to all the 87 DEM pairs of successive DEMs (88 DEMs in total). The time intervals between successive DEMs vary from 6 to 13 min (average: 7 min) except during the breaks used to re-level the robotic total station. Then, the resulting time intervals are longer and vary between 17 and 51 min (average: 23 min, 10 DEM pairs).

A higher survey time resolution requires a higher survey space resolution so that apparent bedform displacements are long enough for cross-correlation. To get sufficiently long (at least one or two pixels) pattern displacements between successive DEMs, DEM grayscale images are resampled to a resolution of 6.25 cm per pixel using the bicubic interpolation function implemented in Fudaa-LSPIV. Bicubic interpolation is often used in image processing to get smoother surfaces than what other interpolation methods like bilinear interpolation or nearest-neighbor interpolation provide. As a result, LSPIV cross-correlation applied to DEM images resampled using the bicubic interpolation function is more likely to detect smoothed, large-scale bedform features rather than local details or noise, hence providing real bedform displacement at the proper scale. Though we were prevented from doing so owing to data availability, gridding the initial survey point data at the resolution required by the pattern matching would have been a better option than resampling the available 25 cm-resolved DEMs to

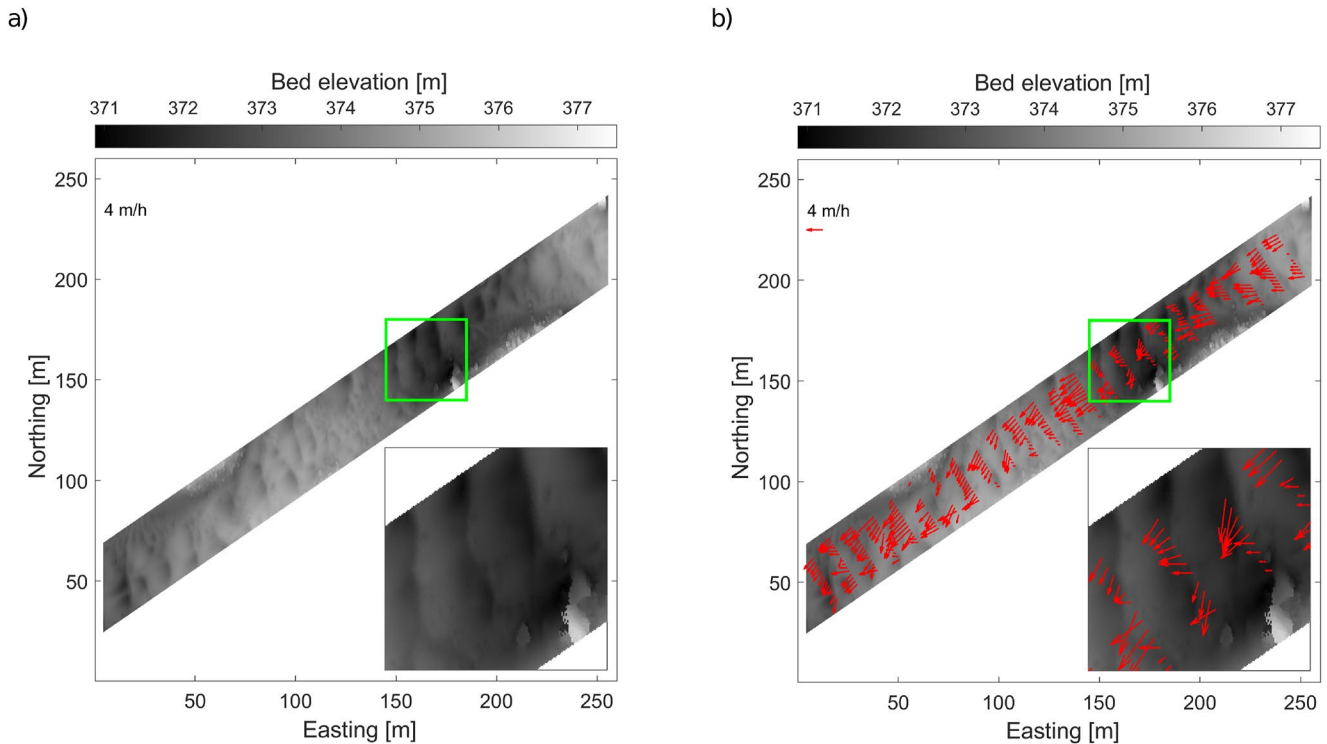


Figure 3. LSPIV application: 256 grayscale-level bed elevation map (first DEM, a) and instantaneous bedform velocity field (first DEM pair, b). Northing and Easting values in this and subsequent figures are relative to the same local horizontal datum.

a higher resolution (6.25 cm). The raw data would be appropriate for such high-resolution gridding as Leary and Buscombe (2020) state that they provide “up to 1,000 individual soundings per square meter,” that is, a resolution of 3 cm, approximately.

The computational grid consists of 24 cross-sections perpendicular to the channel centerline with 18 nodes each, that is, 432 nodes in total. The constant LSPIV parameters are adjusted manually to capture the velocity of the largest bedforms (i.e., the dunes), not the velocity of local sediment patterns that may move with different velocities. The size of the square interrogation areas is set to 96 pixels (i.e., 6 m). This size is set large enough to include identifiable patterns corresponding to the expected scale of bedforms, but small enough to capture local bedform movements over the width and length of the channel. The size of the search area is set to 24 pixels (i.e., 1.5 m) in the West and South directions and zero otherwise. This distance is longer than dune displacements manually checked in the subset of the DEM pairs with the longest time intervals.

As Fudaa-LSPIV cannot accommodate variable time steps between successive images, an arbitrary time step was set and the actual instantaneous velocities V_b in m/h has to be computed outside Fudaa-LSPIV from displacement results in pixels (cf. Figure 3b). The time interval between DEMs should be short enough so that patterns do not change their shape and remain identifiable through cross-correlation. As the velocity results have high correlation levels indeed, the minimum admissible correlation is set to 0.85 to filter out spurious results. Some spurious velocity results with a West component of zero, due to the lack of identifiable patterns, are filtered out during this step. At each node of the computational grid, the time-averaged velocity is calculated as the time-weighted average of instantaneous velocities from DEM pairs.

3.2. Computing Bedform Characteristics Along Local Bedform Velocity Direction

From the bed elevation profile interpolated along bedform celerity direction, the bedform characteristics could be computed using a range of existing methods and tools (cf. van der Mark & Blom, 2007). However, different methods applied to the same DEM data are not expected to detect the same population of bedforms and produce the same results since their assumptions and thresholds are different (van der Mark et al., 2008). We have developed

a semi-automated method especially designed to detect bedforms similar to those producing the pattern displacements used to establish the LSPIV bedform velocities. In the case of the campaign of July 2015, the LSPIV interrogation area (6 m) was sized large enough to track the movement of the largest bedforms (dunes longer than 6 m, typically) instead of smaller, superimposed bedforms that may travel at faster speeds. For the same survey, Leary and Buscombe (2020) using the bedform tracking tool (BTT) developed by van der Mark et al. (2008) found an average bedform wavelength of 5.1 m with a large standard-deviation (2.7 m).

For each computation node and each time interval, each DEM in a pair is linearly interpolated along the local bedform velocity direction (cf. Figure 4). The transect lengths are set based on prior estimates of bedform length from visual inspection of the DEMs. We checked that each transect includes at least three individual bedforms to make sure that the ends of the central bedform corresponding to the velocity measurement can be identified. To account for bedform movement, the velocity measurement is located at the start and end of the velocity vector in the first DEM and the second DEM, respectively. The bedform troughs along this transect are automatically detected using the $envelope(x, np, "peak")$ function of Matlab, where x is the input sequence (here, the bed elevations along the transect). This function with the "peak" option determines the envelopes of a curve using spline interpolation over local maxima separated by at least np samples.

The baseline of the bedforms is computed as the linear interpolation of trough elevations along the transect. The closest troughs on the left and on the right of the velocity measurement location define the bedform whose velocity was measured. The corresponding dune cross-section area is computed by integrating the difference between the bed elevation and the baseline from trough to trough. The mean dune height H_b is computed by dividing this area by the horizontal trough to trough distance, or dune length, L_b . The shape factor α_b is computed by dividing H_b by the maximum bed-baseline difference $H_{b,max}$.

The results are sensitive to the sample number np of the $envelope(x, np, "peak")$ function used to detect the bedform troughs. When np is shorter than the bedforms, false troughs may be detected (oversegmentation); when np is longer than the bedforms, troughs may be missed (undersegmentation). As the lengths of bedforms actually vary with space and time, variable np values are selected based on empirical criteria that can be adjusted for each application case. For the present application, troughs and bedform characteristics are computed for several values of np determined from expert judgment to cover a realistic range of bedform sizes: 10, 20, 24, 32, corresponding to 2.5, 5, 6, and 8 m, respectively. An np setting is discarded if the mean bedform height above the baseline is negative. Among the remaining settings, the np value that yields the smallest difference in bedform areas ($\approx H_b \times L_b$) between the two successive DEMs is selected.

Based on the visual inspection of a large number of DEM profiles, such rules for calibrating np for each velocity vector are found to produce acceptable results for the application presented in this paper. Figure 4 shows an example for which a too small np produces a negative mean height above the baseline due to oversegmentation (Figure 4b). With the right np value, the central bedform corresponding to the velocity measurement is correctly segmented in the two successive DEMs with positive mean heights, acceptable baseline slopes, and very similar areas and other bedform characteristics (Figure 4c). This typical example also shows that, even for the right np value, a false trough may remain detected in the downstream or upstream bedforms in a DEM transect because the velocity vectors of these bedforms may differ in direction from that of the central bedform, resulting in projection errors and overestimated length. This problem does not affect the determination of the central bedform characteristics. Other examples illustrating the np selection criteria in other situations are provided as Supporting Information S1. The mean and standard-deviation of the calibrated np values are 18.33 ± 0.51 (i.e., $4.58 \text{ m} \pm 0.13 \text{ m}$), which is consistent with the average bedform wavelength found by Leary and Buscombe (2020) and with the size of the LSPIV interrogation area (6 m). The computational cost of the iterative selection of np is acceptable, as processing the whole data set takes approximately 1 hr on a conventional personal computer when four np values are tested in the iteration.

3.3. Computing Space- and Time-Averaged Bedform Characteristics

The bedform characteristics obtained with the two DEMs in a pair are averaged to assign H_b and α_b values to each velocity result, for each time interval and each node of the computational grid.

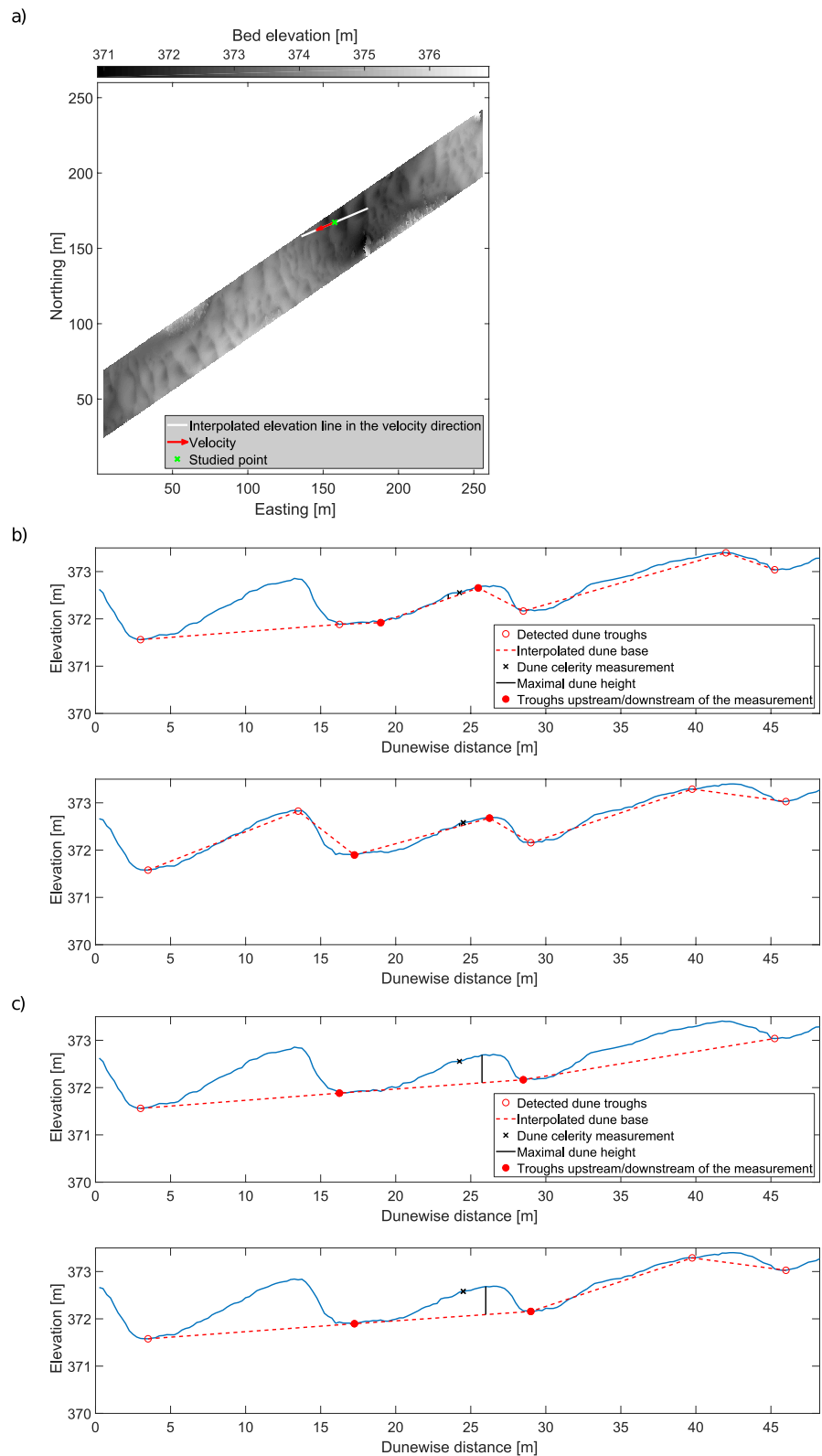


Figure 4. (a) Assigning bedform characteristics to local bedform velocity measurements: first DEM with an example bedform velocity measurement and the corresponding transect line for interpolation; (b) along-velocity interpolated bed profiles for $np = 10$, that is, 2.5 m and $np = 20$, (c) that is, 5 m from successive DEMs (the first on top of the second). Velocity measurement position (LSPIV grid node), detected troughs, interpolated bedform baseline and maximal bedform height, $H_{b,max}$, are indicated.

Simple spatial averages over the $i = 1, \dots, N$ points of the computational grid can be computed for any bedform and bedload parameters. For the bedform characteristics H_b , $H_{b,\max}$, and α_b which are included in the bedload rate computation, velocity-weighted averages may be meaningful:

$$\overline{H_b} = \frac{\sum_{i=1}^N V_{b,i} H_{b,i}}{\sum_{i=1}^N V_{b,i}} \quad (3)$$

$$\overline{H_{b,\max}} = \frac{\sum_{i=1}^N V_{b,i} H_{b,\max,i}}{\sum_{i=1}^N V_{b,i}} \quad (4)$$

$$\overline{\alpha} = \frac{\sum_{i=1}^N V_{b,i} \alpha_{b,i}}{\sum_{i=1}^N V_{b,i}} = \frac{\overline{H_b}}{\overline{H_{b,\max}}} \quad (5)$$

Compared to simple spatial averages, these “bedload-based” averages give more weight to the locations where bedload is more active. Indeed, the weighting coefficients $V_{b,i}$ in Equations 3–5 for bedload-based averages become equal to 1 when computing spatial averages. Time-averaged bedform characteristics are computed as a time-weighted average, to account for the variable time intervals separating successive DEMs. Thus, results have a weight proportional to the time intervals.

3.4. Computing Bedload Fluxes and Bed Evolution

For each computational node and each time interval, the local, instantaneous bedload rate vector \vec{q}_b (in m^2/s) is computed from bedform velocity V_b and mean height H_b by solving Equation 1 with $p = 0.35$ and $q_{b,0} = 0$ (the same values were fixed by Leary and Buscombe (2020)). The time-averaged bedload rate is computed as the time-weighted average of instantaneous bedload rate from all the time intervals of the survey. As bedform velocity is solved in two dimensions, bedload rates are also mapped in two dimensions, which is the main purpose of the proposed method.

The cross-sectional-integrated flux Q_b (in kg/s) through each of the 24 transects of the LSPIV computational grid is computed by integrating the normal components of the local bedload rates $\vec{q}_{b,i}$ along the transect with nodes i . Following a mid-section procedure, the elemental bedload flux $Q_{b,i}$ through the segment of transect around node i is computed as:

$$Q_{b,i} = 0.5\rho_s \left(\vec{q}_{b,i} \times \vec{d} \right) \cdot \vec{k} = 0.5\rho_s [q_{b,x,i}(y_{i+1} - y_{i-1}) - q_{b,y,i}(x_{i+1} - x_{i-1})] \quad (6)$$

where ρ_s is the sediment density, $\vec{q}_{b,i} = (q_{b,x,i}, q_{b,y,i}, 0)$ is the local bedload rate vector, $\vec{k} = (0, 0, 1)$ is the unit vertical vector, $\vec{d} = (x_{i+1} - x_{i-1}, y_{i+1} - y_{i-1}, 0)$ with (x_i, y_i) the coordinates of node i in the horizontal plane.

Missing values are linearly interpolated from the nearest neighbors along the same transect. By construction of the computational grid, as the IA overlaps the edge of the DEM, local bedload cannot be computed at the extreme nodes of each transect. Near-edge bedload fluxes are constantly extrapolated from the nearest measured values. The total flux Q_b through a transect is simply computed as the sum of all the elemental fluxes $Q_{b,i}$ of the transect.

The change in mean bed elevation over the domain between each of the 23 transect pairs is computed following two independent procedures. First, the mean elevation difference Δh_{DEM} is computed from the difference of the two successive DEMs. Alternatively, the mean elevation difference Δh_{flux} is computed from the mass continuity over the domain of area A during time interval Δt :

$$\Delta h_{\text{flux}} = \frac{(Q_{b,\text{in}} - Q_{b,\text{out}})\Delta t}{(1 - p)A} \quad (7)$$

where $Q_{b,\text{in}}$ and $Q_{b,\text{out}}$ are the bedload flux input and output, respectively. The former estimate (Δh_{DEM}) will be called the “observed” bed-elevation change while the latter estimate (Δh_{flux}) will be called the “computed” bed-elevation change. Their comparison will inform on the consistency of bedload velocity, rate and flux measurements.

Table 1
Bedform Characteristics Deduced From the Method Presented in This Paper and Comparison With Those Reported in Leary and Buscombe (2020)

Variables	Units	Simple average (mean \pm std)	Bedload-based average (mean \pm std)	Leary and Buscombe (2020) (mean \pm std)
L_b	[m]	9.2 ± 0.31		5.1 ± 2.7
$H_{b,max}$	[m]	0.42 ± 0.032	0.30 ± 0.041	
α_b	[-]	0.47 ± 0.0077	0.63 ± 0.041	0.50 (assumed)
H_b	[m]	0.21 ± 0.018	0.19 ± 0.019	0.36 ± 0.20
V_b	[m/h]	2.2 ± 0.51		
q_b	[m ³ /s/m]	$7.7 \times 10^{-5} \pm 2.0 \times 10^{-5}$		

4. Results

4.1. Measured Bedform Characteristics

Table 1 shows the bedform characteristics deduced from the method (simple average and bedload-based averages, cf. Section 3.3) and compares those values with those reported by Leary and Buscombe (2020) obtained using the BTT developed by van der Mark et al. (2008) over a smaller central region of the same DEM data set. As expected, different methods produce different bedform characteristics. Our bedform length L_b estimates are significantly higher and less scattered than those found by Leary and Buscombe (2020). As already discussed, the smaller bedforms that do not contribute to the bedform velocities detected by the cross-correlation of 6 m square patterns are not detected by the proposed method. The small standard deviation of bedform lengths (0.31 m) suggests that the population of the longest bedforms is relatively uniform. Other differences may be due to the different regions of the DEM used and to the different directions (streamwise vs. local) of the bed-elevation profiles. However, some tests (not shown) show that such effects cannot be the reasons for the observed differences in the results.

The mean bedform heights H_b (either simple average or bedload-based average) are significantly smaller and much less scattered than those reported by Leary and Buscombe (2020). The shape factors α_b are consistent with the triangular-shape assumption made by Leary and Buscombe (2020). The bedload-based average ($\alpha_b = 0.63$) however is higher than 0.5 and the simple average (0.47), which suggests that the bedforms mainly contributing to bedload, such as those depicted in Figure 4, are more convex than the others. Indeed, the bedload-based average gives more weight to the α_b coefficients of the bedforms with higher velocity, compared to the simple average, as explained in Section 3.3.

Figure 5 shows the relations between dune height, velocity, length, and shape-factor estimates from all DEM pairs and all computational nodes. Bedform velocity seems to be poorly correlated with other bedform characteristics. The most significant correlation appears between $H_{b,max}$ and L_b : longer dunes seem to be generally higher, which is reasonable. Correlations with the shape factor α_b are weaker, suggesting that the bigger bedforms are more convex.

4.2. Comparison With Bedform Models

The observed bedform characteristics can be compared with those predicted by empirical models such as those proposed by Yalin (1964) or van Rijn (1984) for equilibrium dunes. These authors showed that the dune wavelength is mainly controlled by the water depth whereas the dune height is controlled by both the dimensionless bed shear stress (or Shields number) and the water depth. To apply these models, we considered the water depths ($h = 9.5 \pm 0.4$ m) and bed-sand data reported in Section 2.2. We evaluated the roughness height as $k_s = 2d_{84} = 0.82$ mm (Camenen et al., 2019). The cross-section-averaged velocity $U = Q/S_w$, with S_w the wetted area, is $U = 1.15 \pm 0.07$ m/s for the mean discharge of 566 m³/s. The slight decrease of U with discharge during the survey is neglected. From U and k_s , we evaluated the skin-friction Shields number (cf. Camenen et al. (2014)) as $\theta = 0.39 \pm 0.04$ for this discharge.

Figure 6 presents the results for the bedform wavelength L_b and the bedform steepness $\lambda_b = H_{b,max}/L_b$. Our data from Above Diamond Creek are represented with error bars corresponding to the min-max range of bedform and

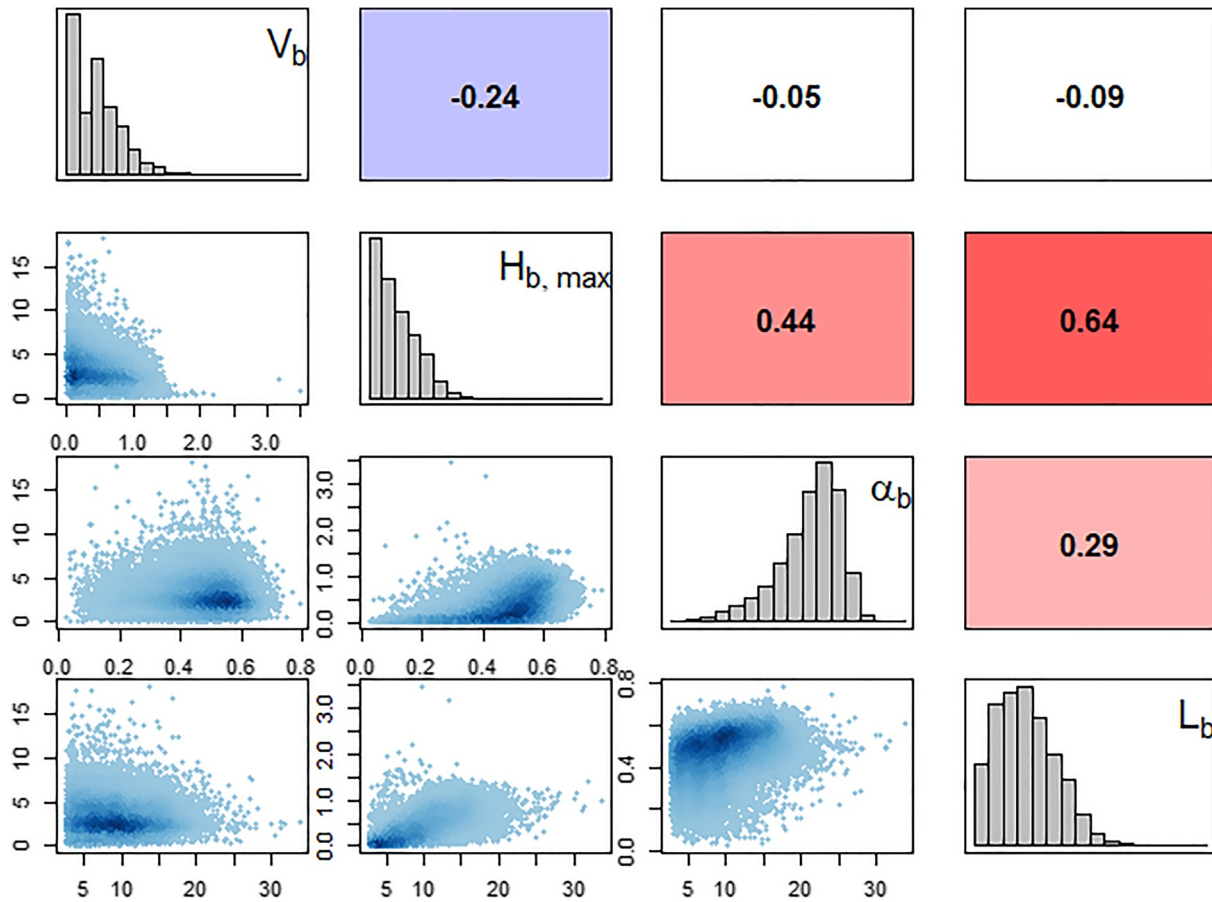


Figure 5. Scatterplot and correlation plot (all instantaneous values at all nodes) of dune velocity [m/h], maximal dune height [m], shape factor [-] and dune length [m]. The values of the axis labels are expressed in m/s for V_b , in m for $H_{b,max}$ and L_b , and without units for α_b .

flow characteristics during the survey. The experimental data collected by Bradley and Venditti (2017) (restricted to grain size $0.2 < d_{50} < 0.5$ mm) as well as those collected by Gualtieri et al. (2020) on the Amazon River are also plotted. The bedform height is similar to, although smaller than, the estimate for equilibrium dunes; however the bedform wavelength is 5 times smaller (cf. Figure 6a) and the bedform steepness is two or 3 times greater

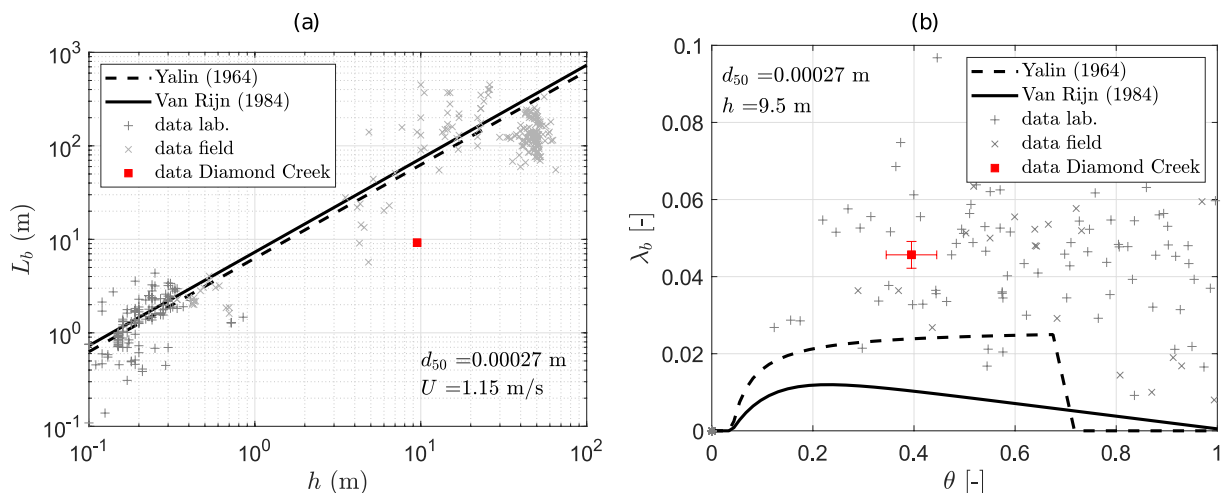


Figure 6. (a) Comparison of observed bedform characteristics and empirical models: bedform wavelength L_b versus water depth h and bedform steepness λ_b (b) versus the Shields number θ .

(cf. Figure 6b). Yalin (1964) and van Rijn (1984) observed that the wavelength to flow depth ratio was $L_b/h \approx 7$ for equilibrium dunes whereas we found $L_b/h \approx 1$. The ratio reported by Leary and Buscombe (2020) for the same data set is even smaller ($L_b/h \approx 0.5$). This specific case would correspond to the lower bound of the range of L_b/h ratios (between 1 and 15) observed by Venditti (2013) in the data set of Allen (1982), or by Bradley and Venditti (2017) and Gualtieri et al. (2020). As observed by Naqshband et al. (2014), bedform wavelengths increase with the Froude number and L_b/h ratios are usually found to be smaller for large rivers. Despite the relatively short bedform length, the bedform steepness that we observe ($\lambda_b = 0.046$) lies within the range of values ($0.015 \leq \lambda_b \leq 0.10$) observed in large rivers by Julien and Klaassen (1995). Compared to the data set collected by Bradley and Venditti (2017) however, the observed steepness values appear quite high and more similar to laboratory data for relatively high Froude numbers. Indeed, Bradley and Venditti (2017) found $\lambda_b = 0.025$ on average, not far from Yalin (1964) model.

The discrepancy between our bedform characteristics and the values predicted by empirical models calibrated in equilibrium conditions may be due to the relaxation time effects in fluctuating flows. As observed by Myrow et al. (2018), unsteady, non-uniform flows induce disequilibrium between the flow and the bed dynamics. During several flood events in various sections of the Dutch Rhine River, during which the discharge varied by a factor 2, Wilbers and Ten Brinke (2003) observed correlations between bedform characteristics and the Shields number, suggesting that bedforms adapt to changes in flow. However, they also reported substantial hysteresis in the velocity, height and length of bedforms during the rising and falling limbs of the floods, suggesting that sediment transport was slightly out of equilibrium. Guala et al. (2020) also argued that the decreasing discharge could imply an underestimation of the bed shear stress that initiated and advected the bedforms under higher discharge conditions at the beginning of the survey. Bed shear stress is indeed directly related to water depth. This could explain why the bedform heights are slightly overestimated by the empirical models, however not why the bedform lengths are so much overestimated.

Another reason why the predicted bedforms are too long and too high may be that the total boundary shear stress derived from the observed mean velocity for the given flow depth is not only produced by bed-roughness elements but also by the channel-scale drag, for example, due to channel expansions and contractions, as observed by Wiele and Smith (1996) and Topping et al. (2007) for the Colorado River, in the same vein as the flume observations by Crickmore (1970). Because the boundary shear stress, hence the Shields number is too high, the predicted bedforms may be larger than the real ones to compensate for the missing channel-scale drag. The limited accuracy of such modeling results underscore the need for continuous observation of bedforms and flow conditions, a more accurate estimation of the Shields number and the development of better models, including dynamical models.

Using our estimated Shields number, we applied semi-empirical bedload transport formulas to compare the results from these equations with those from our bedform tracking method. For example, the Meyer-Peter and Müller (1948) formula and the van Rijn (1984) formula would yield $q_b = 3.0 \times 10^{-5} \text{ m}^3/\text{s}/\text{m}$ and $q_b = 5.3 \times 10^{-5} \text{ m}^3/\text{s}/\text{m}$, respectively. These values are slightly lower than the bedload rate derived from our bedform tracking method ($7.7 \times 10^{-5} \pm 2.0 \times 10^{-5} \text{ m}^3/\text{s}/\text{m}$, cf. Table 1). For comparison, Ashley et al. (2020) found a bedload decreasing from 8 to 5 kg/s on the whole section during the experiment on July 12th, that is, from 5 to $3 \times 10^{-5} \text{ m}^3/\text{s}/\text{m}$, assuming that the active width is $W_a = 64 \text{ m}$.

4.3. Temporal Variability

To evaluate temporal variability, the results spatially averaged over the LSPIV grid of each DEM pair were plotted through time over the duration of the bed elevation survey (Figure 7), along with discharge Q and suspended-sand concentration downloaded from the GCMRC database (https://www.gcmrc.gov/discharge_qw_sediment/). Bedload rate q_b presents a decreasing trend and is roughly halved between the start and end of the survey. This appears to be due to a corresponding decrease in mainly bedform velocity V_b , and also to a less pronounced decrease in mean height H_b . Overall, suspended-sand concentration and bedload rate follow a similar decrease, dropping by approximately 50% after 16:00 when discharge decreases below $\sim 550 \text{ m}^3/\text{s}$.

The shape factor α_b and length L_b show negligible variability over the duration of the bed-elevation survey. These results suggest that the decreasing discharge mainly induced a decrease in bedform velocity and, to a lesser extent,

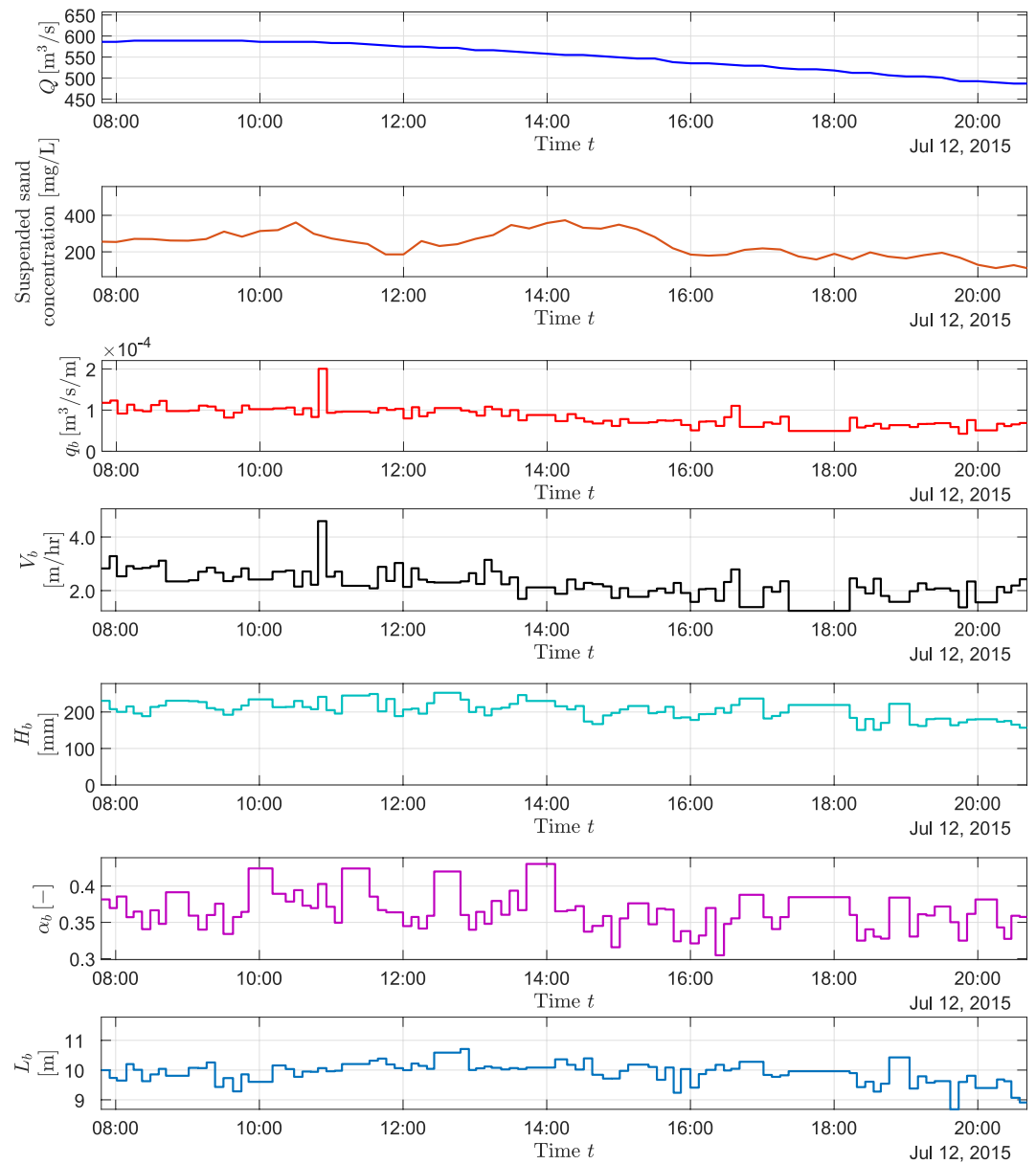


Figure 7. Time evolution of spatially averaged variables during the acoustical mapping survey: water discharge Q and suspended-sand concentration measured at the gage, bedload rate q_b , bedform velocity V_b , mean bedform height H_b , shape factor α_b and length of the bedform L_b . Bedload-based averages are presented for H_b and α_b (see Section 3.3 for explanations). The results are plotted as plateaus over the time intervals between the first and second DEM in a pair.

in bedform mean height while the shape factor and wavelength remained relatively constant. This temporal trend was similarly noticed by Leary and Buscombe (2020).

4.4. Bedload Dynamics

Mapping the time-averaged bedform and bedload characteristics over the Colorado River reach illustrates the spatial variability in the bedform dynamics at our study site (Figure 8). Spatial patterns in mean bedform height H_b clearly appear with heights up to 0.7 m in the narrower portion of the channel constricted by rocks (Figure 8a). Zones with very low bedforms ($H_b < 0.1$ m, typically) are located near and downstream from fans of colluvium shed from the canyon walls. Overall, wide, laterally homogeneous cross-sections located at both the upstream

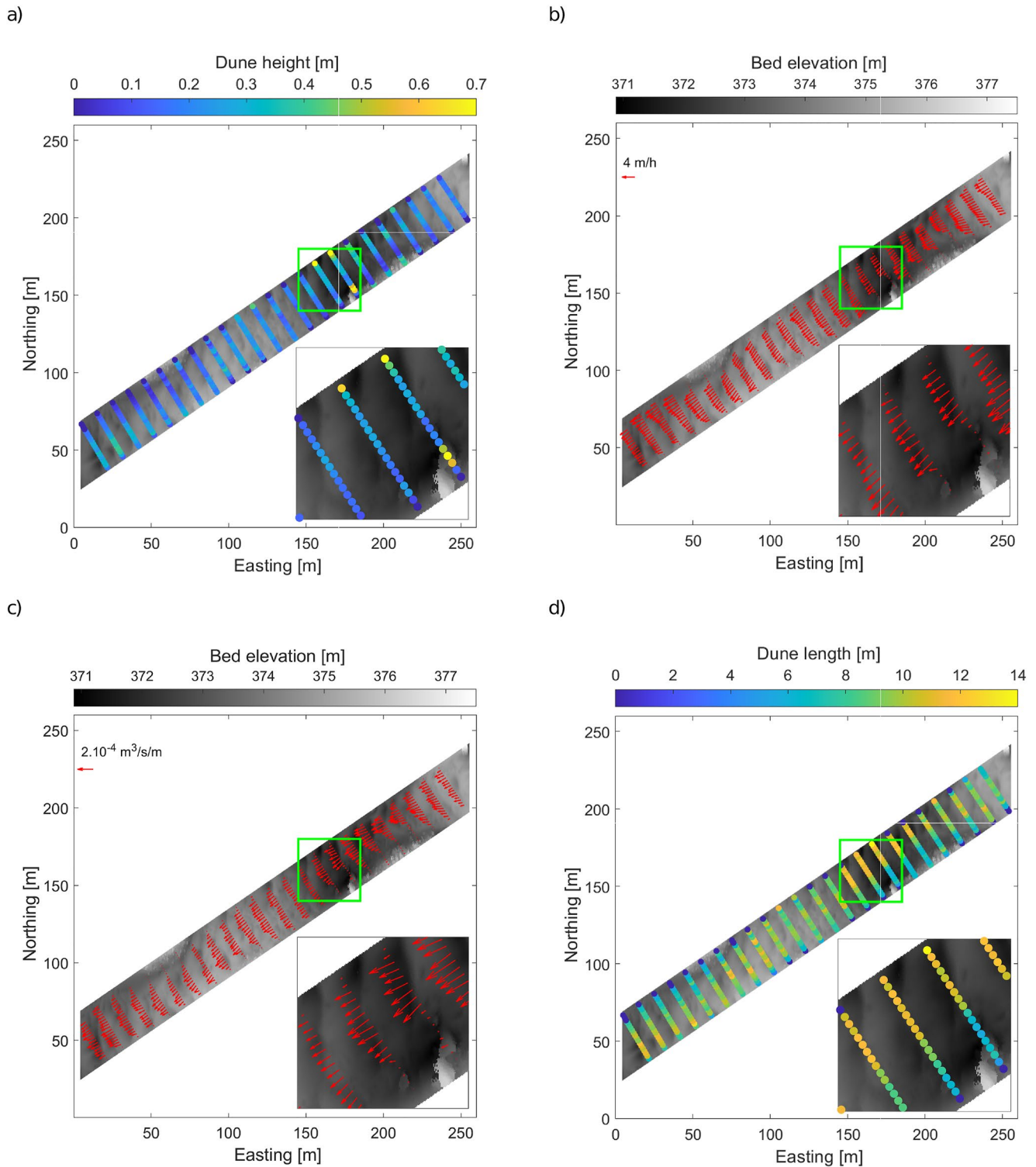


Figure 8. Maps of (a) time-averaged mean bedform height, (b) time-average bedform velocity, and (c) time-averaged bedload rates and (d) time-average bedform length.

and downstream ends and in the middle of the reach have flatter bedforms than do narrower cross-sections. This behavior results in slightly different spatial distributions of time-averaged bedform velocities V_b (Figure 8b) and bedload rates (Figure 8c), which are often less uniform laterally than bedform velocities. Bedload rates seem positively correlated with bedform wavelengths (Figure 8d).

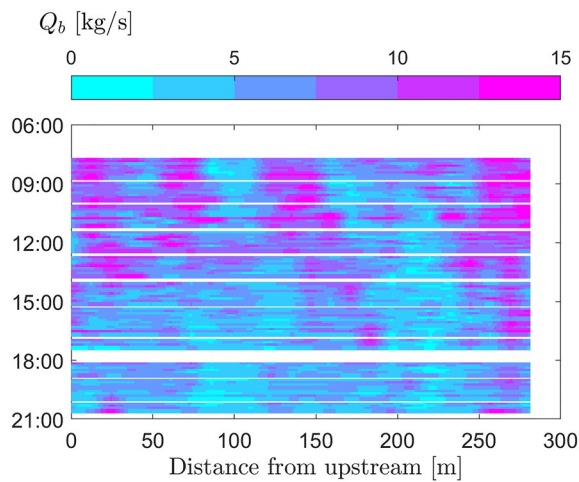


Figure 9. Time-evolution of the instantaneous cross-section-integrated bedload fluxes Q_b along the reach.

and DEM-based approaches indicate a small amount of bed erosion, with very close estimates of the cumulative change in bed elevation: -9.0 mm and -9.4 mm, respectively. Such overall agreement suggests that the flux estimation through the proposed dune-tracking method is not significantly biased. However, instantaneous and local estimates of bed evolution are too uncertain to capture the very small differences. The root-mean-square error (RMSE) and the mean absolute error between Δh_{flux} and Δh_{DEM} are 64 mm/hr and 39 mm/hr, respectively, which is relatively large compared to the observed variations of the bed-evolution rates (cf. Figure 10). This issue relates to the spatial resolution of the estimation, that is, the distances between successive transects along the reach which should be short enough to highlight the dynamics of each part of the reach but not shorter than the bedform length. In our case, the longitudinal distance between transects is around 12 m, namely 1.3 times the mean bedform length. This short distance might induce some of the variability in the computed and observed bed-evolution rates along the reach.

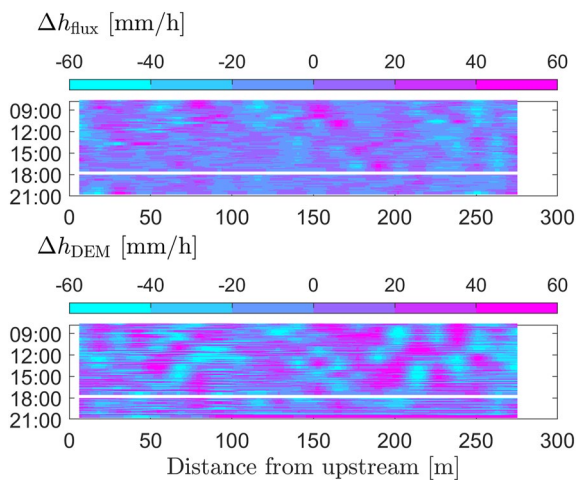


Figure 10. Time-evolution of the computed (Δh_{flux}) and observed (Δh_{DEM}) bed-evolution rates along the reach.

Longitudinal variations of bedload rates (Figure 8b) arise as a combination of longitudinal variations of velocities (mainly) and dune heights. Longitudinal trends in the cross-sectional-integrated bedload flux Q_b over the reach can be seen in Figure 9. Despite the relatively large uncertainty and variability of the bedload flux estimates, longitudinal fluctuations and their time evolution appear to correlate with the bedform wavelength and migration rate, respectively. As already observed, bedload intensity decreases through time due to the simultaneous discharge decrease.

4.5. Comparison With the Observed Bed Evolution

The bedload-flux estimation allows for sediment budgeting along the reach and quantitative comparisons with DEM differences over the surveyed period of time. Positive and negative bedload gradients should be related to zones of aggradation and degradation, respectively. Again, consistent spatial and temporal trends in both the computed (Δh_{flux}) and observed (Δh_{DEM}) bed-evolution rates over the survey period are visible (Figure 10). The signals are affected by substantial noise, and the amplitude of Δh_{DEM} patterns is much higher than the amplitude of Δh_{flux} patterns.

The cumulative bed evolution profiles (not shown) for both methods are virtually zero along the whole reach. On average over the reach, both flux-based and DEM-based approaches indicate a small amount of bed erosion, with very close estimates of the cumulative change in bed elevation: -9.0 mm and -9.4 mm, respectively. Such overall agreement suggests that the flux estimation through the proposed dune-tracking method is not significantly biased. However, instantaneous and local estimates of bed evolution are too uncertain to capture the very small differences. The root-mean-square error (RMSE) and the mean absolute error between Δh_{flux} and Δh_{DEM} are 64 mm/hr and 39 mm/hr, respectively, which is relatively large compared to the observed variations of the bed-evolution rates (cf. Figure 10). This issue relates to the spatial resolution of the estimation, that is, the distances between successive transects along the reach which should be short enough to highlight the dynamics of each part of the reach but not shorter than the bedform length. In our case, the longitudinal distance between transects is around 12 m, namely 1.3 times the mean bedform length. This short distance might induce some of the variability in the computed and observed bed-evolution rates along the reach.

5. Conclusion

The method introduced in this paper aims at computing local bedload components from successive, high-resolution DEMs of a river reach with migrating bedforms. The method combines cross-correlation velocimetry (LSPIV) and computation of bedform characteristics along their direction of travel. While other methods could be used for determining the bedform characteristics from the interpolated bed-elevation profiles, a semi-automated troughs and crests detection method is implemented to ensure that the velocities and heights are computed from the same bedforms. The method is successfully applied to an approximately 300-m long reach of the Colorado River in Grand Canyon upstream from Diamond Creek. The distributions of the bedform velocities, heights, lengths and shape factors can be studied and compared with experimental data from the literature. While the bedform characteristics are consistent with the data from rivers in the literature, they are poorly predicted by classical bedform models based on equilibrium conditions, likely due to unsteady flow and disequilibrium sediment-transport conditions. The results provide high-resolution insight on the spatial and temporal dynamics of bedforms, evidencing a clear decreasing trend of all bedform parameters with decreasing discharge and suspended-sand concentration, and the influence of local channel non-uniformity on the spatial distribution of two-dimensional

bedload rates and fluxes. The latter are found to be consistent with the bed evolution derived from DEM differences, suggesting that the results from the proposed method are unbiased.

Since the method is general, it can be applied to other pairs of high-resolution DEMs acquired in other river systems. The central idea of establishing the bed-elevation profiles along the local bedform velocities, instead of a fixed direction along the channel or main flow, can be introduced in other existing bedform-tracking methods, provided that the local velocities are computed. The original method implemented for detecting the bedforms and measuring their main characteristics appears to be efficient in capturing bedforms at a consistent scale, which is needed to measure bedload flux. The method is also useful to produce more detailed observations of bedform dynamics in situations where flow unsteadiness and/or sediment-transport in local disequilibrium with the upstream sediment supply exist. The discrepancy between our observations in the Colorado and bedform models assuming transport equilibrium suggests that actually most of the literature data from real rivers are from such situations. As the method solves bedform velocity and bedload in two dimensions, it could be used to evaluate 2D or 3D numerical models and to quantify diffusive effects usually not measured.

Future applications should be useful to evaluate the accuracy and robustness of the method and its various components. The sensitivity of the bedform velocity measurements to the LSPIV parameters, including time intervals between DEMs and size of interrogation areas, should be evaluated, in relation with the nature of the bed-elevation patterns tracked. The robustness of the bedform detection function, including the automatic selection of the parameter np , the minimal number of samples between local maxima, should be validated for different application cases. Sediment budgets established from bedload flux gradients should be compared with DEM differences in reaches with larger bed evolution than the case study presented in this paper. Also, cross-section-integrated bedload fluxes could be compared with concurrent measurements of bedload or bed-material suspended load (e.g., using samplers or hydroacoustical data). As both the standard use of LSPIV for velocity measurement and our usage for bedform-geometry extraction require high resolution and high accuracy of successive DEMs, experimental and theoretical studies would be useful to quantify the impact of the survey quality on the results, and to establish practical guidelines for an optimal application of the method.

Data Availability Statement

The data set and the data processing algorithm used in this study can be downloaded at this link: <https://doi.org/10.5281/zenodo.7014592>. The Fudaa-LSPIV software is freely available for download here: <https://forge.irstea.fr/projects/fudaa-lspiv/files>. The acoustic survey data were made publicly available by Leary (2018). The data times series recorded at the Above Diamond Creek gage by the USGS Grand Canyon Monitoring and Research Center (GCMRC) are publicly available from their database: https://www.gcmrc.gov/discharge_qw_sediment/.

Acknowledgments

The authors are grateful to Joel Sankey (U.S. Geological Survey) and to three anonymous reviewers for their insightful and helpful comments. This study was conducted within the Rhône Sediment Observatory (OSR), a multi-partner research program funded through the Plan Rhône by the European Regional Development Fund (ERDF), Agence de l'eau RMC, CNR, EDF, and three regional councils (Auvergne-Rhône-Alpes, PACA, and Occitanie). This work received financial and technical support from the Compagnie nationale du Rhône (CNR). Collection of the multibeam sonar measurements used for dune tracking was funded by the U.S. Department of the Interior's Glen Canyon Dam Adaptive Management Program. Any use of trade, product, or firm names is for descriptive purposes only and does not imply endorsement by the U.S. Government.

References

- Abraham, D., Kuhnle, R., & Odgaard, A. (2011). Validation of bed-load transport measurements with time-sequenced bathymetric data. *Journal of Hydraulic Engineering*, 137(7), 723–728. [https://doi.org/10.1061/\(ASCE\)HY.1943-7900.0000357](https://doi.org/10.1061/(ASCE)HY.1943-7900.0000357)
- Allen, J. R. L. (1982). *Sedimentary structures: Their character and physical basis* (1st ed.). Elsevier.
- Ashley, T. C., McElroy, B., Buscombe, D., Grams, P. E., & Kaplinski, M. (2020). Estimating bedload from suspended load and water discharge in sand bed rivers. *Water Resources Research*, 56(2). <https://doi.org/10.1029/2019WR025883>
- Bradley, R., & Venditti, J. (2017). Reevaluating dune scaling relations. *Earth-Science Reviews*, 165, 356–376. <https://doi.org/10.1016/j.earscirev.2016.11.004>
- Camenen, B., Dramais, G., Le Coz, J., & Topping, D. (2019). Continuous sand-transport estimation on the Colorado River. In *Proceedings of 11th symposium on river, coastal and estuarine morphodynamics*.
- Camenen, B., Le Coz, J., Dramais, G., Peteuil, C., Fretaud, T., Falgon, A., et al. (2014). A simple physically-based model for predicting sand transport dynamics in the Lower Mekong River. In A. J. Schleiss, G. de Cesare, M. J. Franca, & M. Pfister (Eds.), *River flow, proceedings of the 7th international conference on fluvial hydraulics* (pp. 2189–2197).
- Claude, N., Rodrigues, S., Bustillo, V., Bréhéret, J.-G., Macaire, J.-J., & Jugé, P. (2012). Estimating bedload transport in a large sand-gravel bed river from direct sampling, dune tracking and empirical formulas. *Geomorphology*, 179, 40–57. <https://doi.org/10.1016/j.geomorph.2012.07.030>
- Crickmore, J. M. (1970). Effect of flume width on bed-form characteristics. *Journal of the Hydraulics Division*, 96(2), 473–496. <https://doi.org/10.1061/JYCEAJ.0002333>
- Dinehart, R. (2002). Bedform movement recorded by sequential single-beam surveys in tidal rivers. *Journal of Hydrology*, 258(1–4), 25–39. [https://doi.org/10.1016/S0022-1694\(01\)00558-3](https://doi.org/10.1016/S0022-1694(01)00558-3)
- Fujita, I., Muste, M., & Kruger, A. (1998). Large-scale particle image velocimetry for flow analysis in hydraulic engineering applications. *Journal of Hydraulic Research*, 36(3), 397–414. <https://doi.org/10.1080/00221689809498626>
- Guala, M., Heisel, M., Singh, A., Musa, M., Buscombe, D., & Grams, P. (2020). A mixed length scale model formigrating fluvial bedforms. *Geophysical Research Letters*, 47(2019GL086625), 1–10. <https://doi.org/10.1029/2019GL086625>

- Gualtieri, C., Martone, I., Filizola Junior, N. P., & Ianniruberto, M. (2020). Bedform morphology in the area of the confluence of the Negro and Solimões-Amazon rivers, Brazil. *Water*, *12*(6), 1–21. <https://doi.org/10.3390/w12061630>
- Hoekstra, P., Bell, P., van Santen, P., Roode, N., Levoy, F., & Whitehouse, R. (2004). Bedform migration and bedload transport on an intertidal shoal. *Continental Shelf Research*, *24*(11), 1249–1269. <https://doi.org/10.1016/j.csr.2004.03.006>
- Jodeau, M., Bel, C., Antoine, G., Bodart, G., Le Coz, J., Faure, J.-B., et al. (2020). New developments of FUDAA-LSPIV, a user-friendly software to perform river velocity measurements in various flow conditions. In *IAHR river flow 2020 conference*. <https://doi.org/10.1201/b22619-120>
- Julien, P., & Klaassen, G. (1995). Sand-dune geometry of large rivers during floods. *Journal of Hydraulic Engineering*, *121*(9), 657–663. [https://doi.org/10.1061/\(asce\)0733-9429\(1995\)121:9\(657\)](https://doi.org/10.1061/(asce)0733-9429(1995)121:9(657))
- Kaplinski, M., Hazel, J. E., Grams, P., Kohl, K., Buscombe, D., & Tusso, R. B. (2017). Channel mapping river miles 29–62 of the Colorado River in Grand canyon national Park U.S. Geological Survey Open-File Report 2017-1030. (pp. 1–35). <https://doi.org/10.3133/ofr20171030>
- Kim, D., Ho, H.-C., Baranya, S., & Muste, M. (2016). Qualitative and quantitative acoustic mapping of bedform dynamics. *Flow Measurement and Instrumentation*, *50*, 80–89. <https://doi.org/10.1016/j.flowmeasinst.2016.06.010>
- Leary, K. (2018). Diamond creek repeat multibeam data. *SEAD Internal Repository*. <https://doi.org/10.5967/M02J6904>
- Leary, K., & Buscombe, D. (2020). Estimating sand bed load in rivers by tracking dunes: A comparison of methods based on bed elevation time series. *Earth Surface Dynamics*, *8*(1), 161–172. <https://doi.org/10.5194/esurf-8-161-2020>
- Le Coz, J., Renard, B., Bonnifait, L., Branger, F., & Le Boursicaud, R. (2014). Combining hydraulic knowledge and uncertain gaugings in the estimation of hydrometric rating curves: A Bayesian approach. *Journal of Hydrology*, *509*, 573–587. <https://doi.org/10.1016/j.jhydrol.2013.11.016>
- Le Guern, J., Rodrigues, S., Geay, T., Zanker, S., Hauet, A., Tassi, P., et al. (2021). Relevance of acoustic methods to quantify bedload transport and bedform dynamics in a large sandy-gravel-bed river. *Earth Surface Dynamics*, *9*(3), 423–444. <https://doi.org/10.5194/esurf-9-423-2021>
- McAlpin, T., Wren, D., Jones, K., Abraham, D., & Kuhnle, R. (2022). Bed-load validation for ISSDOTv2. *Journal of Hydraulic Engineering*, *148*(3). [https://doi.org/10.1061/\(ASCE\)HY.1943-7900.0001968](https://doi.org/10.1061/(ASCE)HY.1943-7900.0001968)
- McElroy, B., & Mohrig, D. (2009). Nature of deformation of sandy bed forms. *Journal of Geophysical Research*, *114*(F3), F00A04. <https://doi.org/10.1029/2008JF001220>
- Meyer-Peter, E., & Müller, R. (1948). Formulas for bed-load transport. In *Proceedings of the 2nd IAHR congress* (pp. 39–64).
- Muste, M., Baranya, S., Tsubaki, R., Kim, D., Ho, H., Tsai, H., & Law, D. (2016). Acoustic mapping velocimetry. *Water Resources Research*, *52*(5), 4132–4150. <https://doi.org/10.1002/2015WR018354>
- Myrow, P., Jerolmack, D., & Perron, J. (2018). Bedform disequilibrium. *Journal of Sedimentary Research*, *88*(9), 1096–1113. <https://doi.org/10.2110/jsr.2018.55>
- Naqshband, S., Ribberink, J. S., & Hulscher, S. J. M. H. (2014). Using both free surface effect and sediment transport mode parameters in defining the morphology of river dunes and their evolution to upper stage plane beds. *Journal of Hydraulic Engineering*, *140*(6), 1–6. [https://doi.org/10.1061/\(ASCE\)HY.1943-7900.0000873](https://doi.org/10.1061/(ASCE)HY.1943-7900.0000873)
- Nittrouer, J., Allison, M., & Campanella, R. (2008). Bedform transport rates for the lowermost Mississippi River. *Journal of Geophysical Research*, *113*(3), F03004. <https://doi.org/10.1029/2007JF000795>
- Rubin, D. M., Topping, D. J., Schmidt, J. C., Hazel, J., Kaplinski, K., & Melis, T. S. (2002). Recent sediment studies refute Glen Canyon Dam hypothesis. *EOS, Transactions of the American Geophysical Union*, *83*(25), 273–278. <https://doi.org/10.1029/2002EO000191>
- Simons, D. B., Richardson, E. V., & Nordin, C. F. (1965). *Bedload equation for ripples and dunes (Professional Paper No. 462-H)*. U. S. Geological Survey.
- Strick, R., Ashworth, P., Sambrook Smith, G., Nicholas, A., Best, J., Lane, S., et al. (2019). Quantification of bedform dynamics and bedload sediment flux in sandy braided rivers from airborne and satellite imagery. *Earth Surface Processes and Landforms*, *44*(4), 953–972. <https://doi.org/10.1002/esp.4558>
- Topping, D. J., Grams, P. E., Griffiths, R. E., Dean, D. J., Wright, S. A., & Unema, J. A. (2021). Self-limitation of sand storage in a bedrock-canyon river arising from the interaction of flow and grain size. *Journal of Geophysical Research: Earth Surface*, *126*(5), e2020JF005565. <https://doi.org/10.1029/2020JF005565>
- Topping, D. J., Rubin, D. M., & Melis, T. S. (2007). Coupled changes in sand grain size and sand transport driven by changes in the upstream supply of sand in the Colorado River: Relative importance of changes in bed-sand grain size and bed-sand area. *Sedimentary Geology*, *202*(3), 538–561. <https://doi.org/10.1016/j.sedgeo.2007.03.016>
- Topping, D. J., Rubin, D. M., Nelson, J. M., Kinzel, P. J., III, & Corson, I. C. (2000). Colorado River sediment transport: 2. Systematic bed-elevation and grain-size effects of sand supply limitation. *Water Resources Research*, *36*(2), 515–542. <https://doi.org/10.1029/1999WR900286>
- Topping, D. J., & Wright, S. A. (2016). *Long-term continuous acoustical suspended-sediment measurements in rivers - Theory, application, bias, and error (Professional Paper No. 1823)*. U. S. Geological Survey.
- Tsubaki, R., Baranya, S., Muste, M., & Toda, Y. (2018). Spatio-temporal patterns of sediment particle movement on 2D and 3D bedforms. *Experiments in Fluids*, *59*(93), 93. <https://doi.org/10.1007/s00348-018-2551-y>
- van den Berg, J. H. (1987). Bedform migration and bed-load transport in some rivers and tidal environments. *Sedimentology*, *34*(4), 681–698. <https://doi.org/10.1111/j.1365-3091.1987.tb00794.x>
- van der Mark, C. F., Blom, A., & Hulscher, S. J. M. H. (2008). Quantification of variability in bedform geometry. *Journal of Geophysical Research*, *113*(F3), F03020. <https://doi.org/10.1029/2007JF000940>
- van der Mark, R., & Blom, A. (2007). *A new and widely applicable tool for determining the geometric properties of bedforms* (Res report Nos. 2007R-003/WEM-002, ISSN 1568-4652). University of Twente. <https://doi.org/10.13140/RG.2.2.17637.40161>
- van Rijn, L. C. (1984). Sediment transport: Part III: Bed forms and alluvial roughness. *Journal of the Hydraulics Division*, *110*(12), 1733–1754. [https://doi.org/10.1061/\(asce\)0733-9429\(1984\)110:12\(1733\)](https://doi.org/10.1061/(asce)0733-9429(1984)110:12(1733))
- Venditti, J. G. (2013). Bedforms in sand-bedded rivers. In J. Shroder & E. Wohl (Eds.), *Treatise on geomorphology* (Vol. 9, pp. 137–162). Academic Press.
- Wiele, S. M., & Smith, J. D. (1996). A reach-averaged model of diurnal discharge wave propagation down the Colorado River through the Grand Canyon. *Water Resources Research*, *32*(5), 1375–1386. <https://doi.org/10.1029/96WR00199>
- Wilbers, A., & Ten Brinke, W. (2003). The response of subaqueous dunes to floods in sand and gravel bed reaches of the Dutch Rhine. *Sedimentology*, *50*(6), 1013–1034. <https://doi.org/10.1046/j.1365-3091.2003.00585.x>
- Yalin, M. S. (1964). Geometrical properties of sand waves. *Journal of the Hydraulics Division*, *90*(5), 105–119. <https://doi.org/10.1061/jyceaj.0001097>
- You, H., Muste, M., Kim, D., & Baranya, S. (2021). Considerations on Acoustic Mapping Velocimetry (AMV) application for in-situ measurement of bedform dynamics. *Frontiers in Water*, *3*, 715308. <https://doi.org/10.3389/frwa.2021.715308>